

Journal of Biomedical Optics

BiomedicalOptics.SPIEDigitalLibrary.org

Characterization of the temperature rise in a single cell during photoacoustic tomography at the nanoscale

Pratik Samant
Jian Chen
Liangzhong Xiang

SPIE.

Pratik Samant, Jian Chen, Liangzhong Xiang, "Characterization of the temperature rise in a single cell during photoacoustic tomography at the nanoscale," *J. Biomed. Opt.* **21**(7), 075009 (2016), doi: 10.1117/1.JBO.21.7.075009.

Characterization of the temperature rise in a single cell during photoacoustic tomography at the nanoscale

Pratik Samant, Jian Chen, and Liangzhong Xiang*

University of Oklahoma, Center for Biomedical Engineering and School of Electrical and Computer Engineering, Stephenson Research and Technology Center, 101 David L Boren Boulevard, Norman, Oklahoma 73072, United States

Abstract. We are developing a label-free nanoscale photoacoustic tomography (nPAT) for imaging a single living cell. nPAT uses a laser-induced acoustic pulse to generate a nanometer-scale image. The primary motivation behind this imaging technique is the imaging of biological cells in the context of diagnosis without fluorescent tagging. During this procedure, thermal damage due to the laser pulse is a potential risk that may damage the cells. A physical model is built to estimate the temperature rise and thermal relaxation during the imaging procedure. Through simulations using finite element methods, two lasers (532 nm at 5 ps pulse duration and 830 nm at 0.2 ps pulse duration) were simulated for imaging red blood cells (RBCs). We demonstrate that a single 5-ps pulse laser with a 400-Hz repetition rate will generate a steady state temperature rise of less than a Kelvin on the surface of the RBCs. All the simulation results show that there is no significant temperature rise in an RBC in either single pulse or multiple pulse illumination with a 532-nm laser with 219 W fluence. Therefore, our simulation results demonstrate the thermal safety of an nPAT system. The photoacoustic signal generated by this laser is on the order of 2.5 kPa, so it should still be large enough to generate high-resolution images with nPAT. Frequency analysis of this signal shows a peak at 1.47 GHz, with frequencies as high as 3.5 GHz still being present in the spectrum. We believe that nPAT will open an avenue for disease diagnosis and cell biology studies at the nanometer-level. © 2016 Society of Photo-Optical Instrumentation Engineers (SPIE) [DOI: [10.1117/1.JBO.21.7.075009](https://doi.org/10.1117/1.JBO.21.7.075009)]

Keywords: photoacoustic imaging; nanoscale photoacoustic tomography; single cell imaging; red blood cells; label-free imaging.
Paper 160181R received Mar. 21, 2016; accepted for publication Jun. 21, 2016; published online Jul. 12, 2016.

1 Introduction

Since the breaking of the diffraction limit through the introduction of super-resolved fluorescence microscopy, optical microscopy has been brought into the nanoscale. It has become possible then to image structures and phenomena at the nanoscale using optical microscopy. The relevance of this achievement is difficult to overstate as it allows for the analysis of an entirely different scale of objects in unprecedented detail, for which these efforts were awarded a Nobel prize. However, super-resolution techniques often rely on fluorescent tagging or the use of external contrast agents for imaging, which results in many disadvantages including, but not limited to, photobleaching, phototoxicity,¹ and small *in vivo* lifetimes.² As a result, there is a very real interest in label-free nanoscale imaging modalities in biomedical settings.³⁻⁶

Photoacoustic tomography (PAT) is a label-free imaging technique that has already seen applications in microscopic imaging. This method circumvents the optical diffraction limit by instead relying on a laser-generated acoustic signal for imaging. PAT has seen applications in vascular biology,⁷⁻⁹ neurobiology,¹⁰⁻¹² dermatology,^{13,14} ophthalmology,^{15,16} and other biological fields since its conception.¹⁷ However, a three-dimensional (3-D) PAT mechanism at the nanoscale has yet to see completion; single-cell PAT has not yet been achieved.

In nanoscale photoacoustic tomography (nPAT), laser-induced thermal excitation generates an ultrasound signal due to thermoelastic expansion. The pulse deposits energy into the specimen, which is partially converted into a detectable acoustic

signal that can be used to reconstruct images. The excitation laser pulse is focused through a lens and achieves its lateral resolution through raster-scanning, similar to that used in PAM. However, nPAT does not rely on the use of a transducer for signal detection or axial resolution. Instead, axial scanning is done through the use of an optical delay line in a pump-probe setup. A laser beam, dubbed the pump beam, is used to generate the photoacoustic (PA) signal, which then travels to the surface of the sample to induce a reflectivity change. At this point in time, another beam, dubbed the probe beam, is reflected off the sample. The change in surface reflectivity can then be used to measure the PA signal instead of relying on an ultrasound transducer. This detection method allows for theoretically infinite bandwidth via the probe beam reflectivity. As a result, nPAT is able to achieve even better resolution than PAM in the axial direction, while matching the resolution of PAM in the lateral directions.

Thermoelastic expansion comes with an associated temperature rise, which must be carefully controlled and accounted for during the imaging procedure.¹⁸ Photothermal cellular damage is a common occurrence following laser irradiation,^{19,20} and high temperature rises have been a concern in similar experiments.¹⁸ It is therefore crucial to demonstrate the thermal safety of nPAT before its implementation in experiment.^{21,22}

Red blood cells (RBCs) are particularly good candidates for imaging via PAT. This is due to the high absorption of hemoglobin at particular excitation wavelengths. The RBC's structure can then be imaged using nPAT, providing high optical contrast

*Address all correspondence to: Liangzhong Xiang, E-mail: xianglzh@ou.edu

with ultrahigh resolution to image the mechanics of the RBC in addition to its hemoglobin concentration distribution. This is especially fortunate because RBC structural characteristics are crucial to their function, and abnormalities are hallmarks of a multitude of diseases, including protist infection, leukemia, and anemia. In addition, the hemoglobin concentration distribution can be analyzed to come to conclusions about the internal operations of the cell in different contexts.²³

In this article, we use finite element methods (FEM) to simulate the temperature rise and signal generation during nPAT of an RBC. FEM has been useful in previous models of photoacoustic absorption and signal generation,²⁴ so we believe that its employment in the context of evaluating thermal safety is capable of providing insight into the feasibility of nPAT. This is a label-free method of obtaining nanoscale images by taking advantage of optical contrast and ultrasonic resolution. We simulate this process using a 532-nm laser at a frequency of 400 Hz with 219 W peak power and 5-ps pulse duration. We also simulate, for the sake of comparison, an 830-nm laser at a frequency of 75 MHz, peak power of 1 kW, and pulse duration of 0.2 ps. These simulations are performed in the interest of demonstrating the feasibility of using this system to image RBCs without thermal damage being a concern, while simultaneously generating a large enough signal to provide high image resolution.

2 Methods

2.1 Red Blood Cell Geometry

Prior to simulation, a mathematical description is needed to visualize and model the RBC shape. To this end, the work of Evans and Fung²⁵ has been crucially important. The biconcave shape with adjustments has been used by several researchers when modeling the RBC for simulative purposes.^{26–28} The general equation of the half-biconcave shape is summarized by Chee et al.²⁹ as follows:

$x = 0.5 \sin \omega$ and $z = [c_0 + c_1 \sin^2 \omega + c_2 \sin^4 \omega] 0.25 D \cos \omega$, where $0 \leq \omega \leq \pi$, $c_0 = 0.207$, $c_1 = 2.003$, $c_2 = -1.123$ and the diameter is given as D . In this article, the diameter is set to $8 \mu\text{m}$ to match a typical healthy RBC.

The above equations yield the half biconcave shape in two dimensions. The 3-D RBC shape can then be modeled as a solid of revolution by rotating the two-dimensional (2-D) shape 2π rad around the z -axis. A mesh for FEM simulation can then be constructed within this shape to allow for 3-D FEM simulations with adjustable spacing. The resulting shape is shown in Fig. 1.

2.2 Physical Model of Temperature

Ultimately, the time evolution of the temperature, $T(x, y, z, t)$, will be described by the 3-D heat equation, which can be solved via finite difference methods. The equation to be solved is as follows:

$$\rho C_p \frac{\partial T}{\partial t} - \nabla \cdot [k \nabla T] = Q_{\text{in}}, \quad (1)$$

where ρ is the density of the material, C_p is the heat capacity at constant pressure, k is the thermal conductivity of the material, and Q_{in} is the incoming heat from the laser. The heat equation is numerically solved using the initial condition that the temperature at all points is equivalent to the average human body temperature (310.15 K). In addition, the RBC exterior was

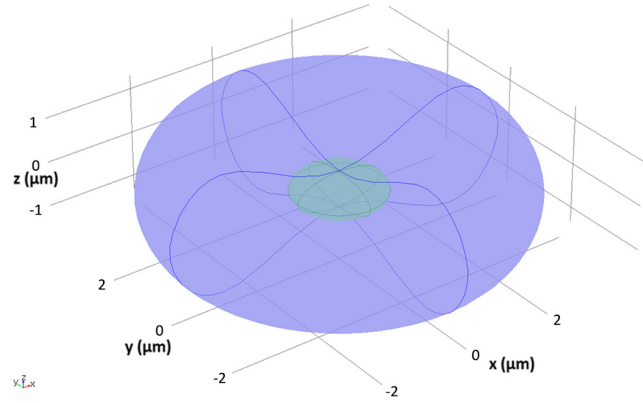


Fig. 1 The 3-D shape of the simulation geometry, laser is incident from the positive z direction. The ellipsoid in the center is the simulated heat source.

maintained at a constant temperature, so the heat flux at the surface could be calculated by applying the standard heat flux equation $q_0 = h(T_{\text{ext}} - T)$, where T is the temperature inside the cell, h is the heat transfer coefficient [taken to be $250 \text{ W}/(\text{m}^2\text{K})$ to match that of water–water], and T_{ext} is the external temperature held constant at 310.15 K.

The laser is introduced to the system in the form of a heat source, depositing heat spatially according to its fluence. We modeled a focused laser to reflect the heat distribution with maximal accuracy. The laser can be incorporated into the system by constructing the source term using the geometrical equations of that of a focused Gaussian beam.

For a Gaussian beam focused at the origin and incoming from the positive z direction, the heat deposited by the laser manifests itself as a source term of the following form:

$$Q_{\text{in}} = Q_0 (1 - R_c) \frac{A_c}{\pi w^2} \left(\frac{w_0}{w} \right)^2 \exp \left[-2 \left(\frac{r}{w} \right)^2 \right] \exp[-A_c(z - z_s)], \quad (2)$$

where w is the beam's spot size parameter and is dependent on z , w_0 is the minimum beam waist size, r is the distance from the beam axis, A_c is the absorption coefficient, R_c is the reflection coefficient, z_s is the z position of the cell membrane that the laser first contacts (to ensure that laser attenuation begins at the correct location), and Q_0 is the incident beam fluence. Equation (2) comes from the intensity profile of a Gaussian beam, which can be multiplied by the absorption coefficient and the absorbance to yield the energy deposited per unit volume by the laser as a function of space. Equation (2) can be multiplied by a time-dependent triangle function as well, therefore simulating a pulsed laser.

The heat source was spatially represented by an ellipsoid in the center of the RBC, as shown in Fig. 1. The a and b semiaxes of this ellipsoid were $0.1 \mu\text{m}$, and the c semiaxis was $0.4 \mu\text{m}$. This ellipsoid was the only source of heat in the system, and Q_{in} was used to calculate the heat deposited at each point in the mesh. Mesh sizing was set to a maximum element size of $0.05 \mu\text{m}$ and a minimum of $0.01 \mu\text{m}$. The mesh was manually made to be much denser in the center region where the heat source ellipsoid was located.

2.3 Acoustic Pressure Model

The PA signal was calculated using FEM coupling several differential equations. This can be calculated by solving three equations simultaneously: the heat equation, the strain equation of motion, and the scalar wave equation in pressure acoustics. These can be coupled by computing the thermal expansion and then computing the resulting pressure wave generated by the RBC membrane. The temperature output of the heat equation is used to compute thermal expansion assuming the RBC interior is a linear elastic material. The thermal expansion is then used with the strain equation to compute the stresses and strains across the RBC. Lastly, the resultant thermal stresses

Table 1 Simulation parameters and temperature calculation.

Parameter	Value
A_c	391.65 cm ⁻¹
R_c	0.005
Numerical aperture	0.7
h	250 W m ⁻² K ⁻¹
k	456 W m ⁻¹ K ⁻¹
ρ (RBC interior)	1125 kg m ⁻³
C_p (RBC interior)	3223.84 J kg ⁻¹ K ⁻¹

Table 2 Simulation parameters and pressure calculation.

Parameter	Value
A_c	391.65 cm ⁻¹
R_c	0.005
Numerical aperture	0.7
h	250 W m ⁻² K ⁻¹
k	456 W m ⁻¹ K ⁻¹
ρ (RBC interior)	1100 kg m ⁻³
C_p (RBC interior)	3223.84 J kg ⁻¹ K ⁻¹
Speed of sound (RBC interior)	1650 m s ⁻¹
Poisson's ratio (RBC)	0.49
Coefficient of thermal expansion (RBC interior)	1.2 × 10 ⁻⁴ K ⁻¹
Young's modulus (RBC interior)	200 Mpa
ρ (Water)	1000 kg m ⁻³
C_p (Water)	4182 J kg ⁻¹ K ⁻¹
Speed of sound (water)	1520 m s ⁻¹
Ratio of specific heats	1

and strains at the surface are fed into the acoustic wave equation, which finally outputs the resultant 2-D pressure distribution.

Initial values for temperature were set to 293.15 K, and the heat source was defined according to the 2-D version of Eq. (2). The simulation was done in 2-D as opposed to 3-D in the interest of computation time, taking advantage of the axial symmetry of the system. In this simulation, the laser pulse was given a Gaussian profile as opposed to the triangle function temporal distribution from the temperature simulations. A full table of parameters can be found in Tables 1 and 2.

3 Results

3.1 Temperature Rise with Single Pulse

The temperature at three probe points [Fig. 2(a)] was observed during the laser illumination. The simulation was run twice with a laser focus at point α [Fig. 2(b)] and at point β [Fig. 2(c)]. In either case, the temperature change in the case of a single pulse was not significant enough to cause thermal damage,³⁰ reaching a maximum value of about 317 K in the single pulse case, which would decay back to very close to the original temperature of 310.15 within a nanosecond. This decay was present when focusing the laser in both the center of the RBC (β) as well as in the case of a focus located at α . The maximal temperature

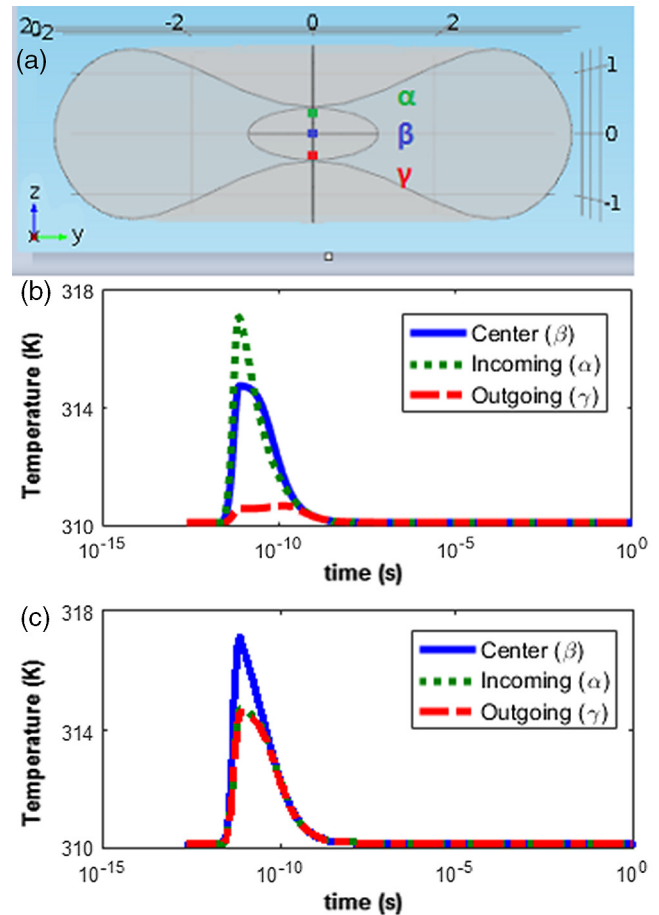


Fig. 2 (a) Probe locations α, β, γ at the origin and at points (0, 0, ± 0.32) within the RBC. Axis scale in μm , laser is incident from positive z direction. (b) Temperature versus time of probe points for a single pulse hitting the RBC focused at α . (c) Temperature versus time for a single pulse hitting the RBC focused at β .

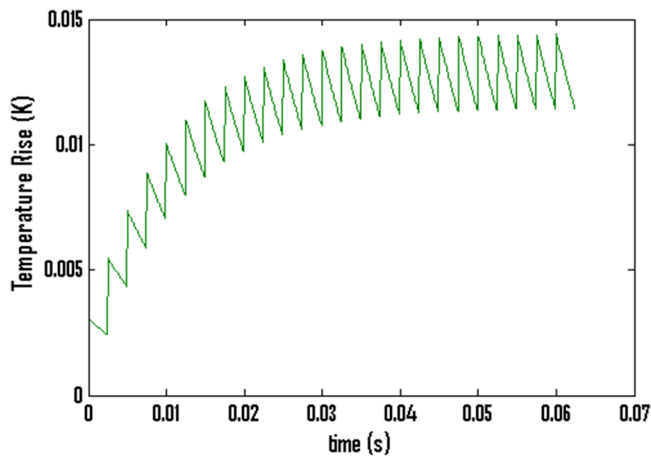


Fig. 3 Steady state temperature at the focus of the laser as a function of time.

at the focus was slightly higher in the case of laser focusing at α as opposed to β . This is to be expected since laser attenuation in Eq. (2) was accounted for with the exponential z -dependent decay, so the laser heat deposition was slightly attenuated upon making contact with the RBC.

3.2 Temperature Rise with High Repetition Rate

The temperature change of repeated pulses is shown in the form of the steady state temperature in Fig. 3. Here the word steady state refers to the final (after a nanosecond has passed) temperature rise observed in the single pulse temperature versus time curves. That is to say, Fig. 3 is the temperature versus time with the ephemeral temperature peaks from laser excitation being omitted. It can be seen that the total increase in steady state temperature is on the order of 0.01 K, which is a guarantee of thermal safety over numerous pulses.³⁰ It can also be seen that the temperature peaks after a certain time has reached; this is due to the heat contribution from earlier pulses diminishing at the same rate that additional pulses heat the system, leading to a steady state equilibrium temperature of <310.165 at the laser focus.

It becomes computationally inefficient to repeat this simulation for extremely high repetition rates on the order of ≥ 1 kHz. Therefore, for systems with higher pulse repetition rates, the steady state temperature will need to be calculated theoretically. Due to the linearity of solutions of the heat equation, the temperature distribution of multiple pulses will simply be the sum of single pulse temperature functions, $T_s(t)$, i.e., the multiple pulse temperature T can be modeled as

$$T = \sum_{i=1}^N T_s(t - it_d),$$

where t_d is the time between pulses, N is the total number of pulses being simulated, and T_s is the single pulse temperature as a function of time.

Then, it is mathematically simple to obtain the multiple pulse temperature evolution given the single pulse temperature evolution by overlapping the output with translated versions of itself. The steady state equilibrium temperature for the laser should be proportional to the pulse repetition rate. This allows us to simulate a single pulse temperature profile that we can overlap to generate a multiple pulse temperature rise.

Using this method, the steady state equilibrium temperature was found of the 219-W picosecond laser with varying repetition rates. It was found that the picosecond laser could reach a repetition rate on the order of 100 kHz without the steady state equilibrium temperature rising significantly (3.5 K for 100 kHz). Thermal damage can be characterized by equivalent minutes at 43°C, which is dependent on exposure time.³¹ The 219-W picosecond laser does not reach 43°C in steady state; it can be concluded that to have temperature rises high enough to cause heat damage (assuming exposure times of a few seconds) to the RBCs, the pulse repetition rate will need to be increased to the order of several hundreds of kHz.

The steady state temperature rise for a femtosecond (830 nm, pulse duration of 0.2 ps, 1 kW fluence, and 75 MHz repetition rate) laser was also examined. The steady state equilibrium temperature was calculated to be 6.3 K. This is much larger than the temperature rise of the 219 W picosecond laser at 400 Hz and even exceeds the theoretical steady state equilibrium temperature of the laser with a 100-kHz repetition rate. As a result, the thermal safety of a 100-kHz laser with a fluence can be more confidently guaranteed as compared with the femtosecond laser at 75 MHz; the exposure time under which thermal safety with this laser can be guaranteed will be lower than that of the picosecond laser. In addition to this, the absorption of hemoglobin at the femtosecond laser wavelength (830 nm) is lower than at the femtosecond laser wavelength (532 nm), so the signal strength per watt of fluence will be weaker with this laser.

3.3 Spatial Distributions of Temperature Rise in a Single Cell

The spatial distribution of the temperature is also relevant and can be analyzed via the generation of volume temperature plots. In the single pulse scenario, it is easiest to analyze the spatial temperature distribution at the peak of the temperature rise. Figure 4 shows the spatial temperature distribution with time with a single pulse illumination. It can be seen that the temperature rise is very localized in a small part around the center of the RBC. This is shown in Fig. 5 where the location of the highest temperature is displayed (the rest of the cell did not see a

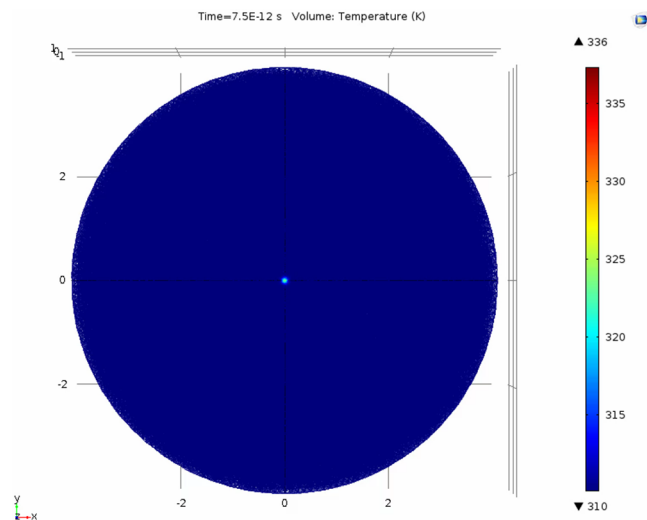


Fig. 4 The spatial distribution of the temperature at the time of peak temperature rise through single pulse illumination. Video 1, MPEG, 1.1 MB [URL: <http://dx.doi.org/10.1117/1.JBO.21.7.075009.1>].

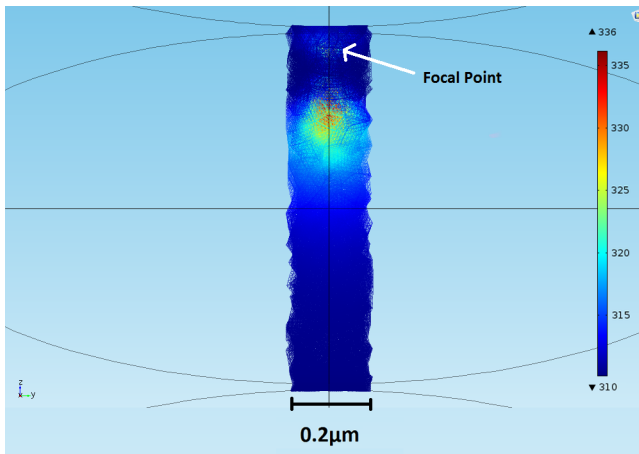


Fig. 5 Peak temperature rise in center region of the RBC after repeated pulsed illumination by laser. Laser is incident from positive z direction. Colorbar legend is in Kelvin.

significant difference from the initial temperature rise at the time of peak temperature at the focus). In this case, it is clear to see that some areas actually exceed the temperature at the focal point, as illustrated by the red coloring. This can be attributed to the fact that the focus lies toward the top of the figure and is not directly in the center; as a result, there is a larger heat sink in the negative z direction than there is in the positive z direction. The positive z portion of Fig. 5 then does not have as large a capability of dissipating incident heat away from peaks. Nevertheless, this peak is still ephemeral and only on the order of a 10-K rise from equilibrium, still not enough to cause thermal damage to the RBC when the duration is taken into account. It can be seen that the change in temperature is localized to the area around the focus, which would explain its fast dissipation and decrease. However, the temperature did not see any significant rise from the equilibrium.

In the case of multiple pulses, it makes the most sense to analyze the maximal equilibrium temperature as opposed to the ephemeral peaks (which were ill-behaved due to the larger

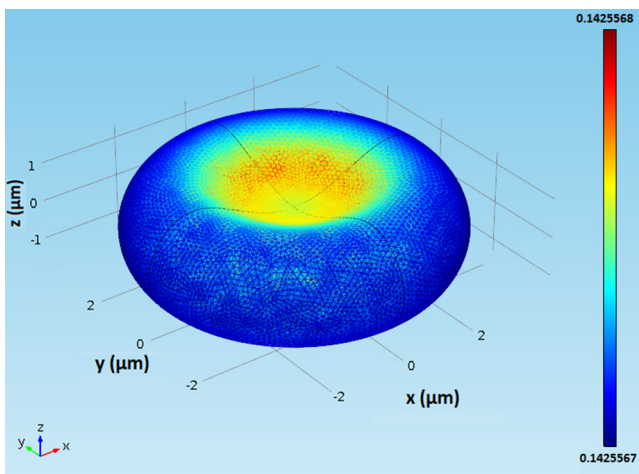


Fig. 6 Spatial distribution of temperature deviation (from initial temperature) immediately following (0.001 s) after the final pulse in the multiple pulse temperature simulation. Colorbar legend is in Kelvin. It is to be noted that the temperature scale here is much finer than that from previous figures, not even covering an entire μK in difference.

time-step size in computing this many pulses). While there is not a drastic change ($\sim 0.1 \mu\text{K}$) in the temperature in this context, it is still useful to illustrate this spatial distribution to analyze the pattern of heat flow in the cell. This is shown in Fig. 6, where it can be seen that the heat dissipates outward from the center and that the ends of the cell remain at the environmental temperature even in the face of a 400-Hz laser. The simulation shows that under repeated irradiation by a laser, the temperature rise in an RBC is $\sim 0.1 \mu\text{K}$, which is not large enough to cause thermal damage in nPAT.

This simulation was also repeated for multiple pulses striking the RBC, such that the temperature evolution could be studied over time. The results are shown in Fig. 3, which shows the relaxation temperature over time as the RBC is hit with a series of laser pulses focused at the green probe point. This temperature did not result in more than a 10 mK change in temperature rise. The peaks did not last longer than single nanoseconds, so they were omitted in the context of data presentation. This data set shows that the temperature at the focus does not show a significant rise during PA imaging and should be indicative of the safety of the nPAT system at the specified fluence levels.

3.4 Signal Generation and Detection

In the 2-D case, the RBC was encased in a coupling medium (which was taken to be water). PA wave amplitude was monitored at a probe point located at (8,0) using the center of the RBC as the origin, as shown in Fig. 7(a). It can be seen in Fig. 7(b) that the generated PA pressure at this probe point from the laser pulse of the same fluence as in the temperature simulations reaches more than 2.5 kPa in magnitude. To properly measure this signal, the noise of the system must be known, but these simulation results show that at this probe point a signal of appreciable magnitude will be generated by the laser pulse.

The composition of the signal can be analyzed via spectral analysis. This is done in Fig. 7(c), which shows the frequency spectrum of the signal. The peak of this frequency spectrum occurs at a frequency of 1.47 GHz, with signals of considerable amplitude at frequencies as high as 3.5 GHz. The axial resolution is given as

$$R_a = 0.88 v_s / f,$$

where v_s is the velocity of sound and f is the frequency.³² Using the speed of sound in water and a frequency as high as 3.5 GHz, yields $R_a \approx 373 \text{ nm}$, which is suitable for nanoscale imaging. The spatial propagation of the PA waves is also important to analyze, and the pressure waves can be represented in a surface plot for particular times. In the context of ensuring that the PA signal from the laser is large enough to measure, the time of highest PA signal amplitude at the probe point is a sensible time at which to examine propagation. A plot of the pressure distribution is given in Fig. 8. The wavefront can be seen after it has propagated outward from the center of the RBC (at which the laser is focused), and the pressure wave is seen to be originating from the center of the cell symmetrically outward.

4 Discussion

To cause thermal damage to biological tissue, the temperature must have an instantaneous rise of $\geq 150 \text{ K}$ or a cumulative temperature rise of 43 K for a sustained period of time.^{31,33,34} Simulations of the temperature change induced by a laser with 219-W peak power show that the temperature rise is not

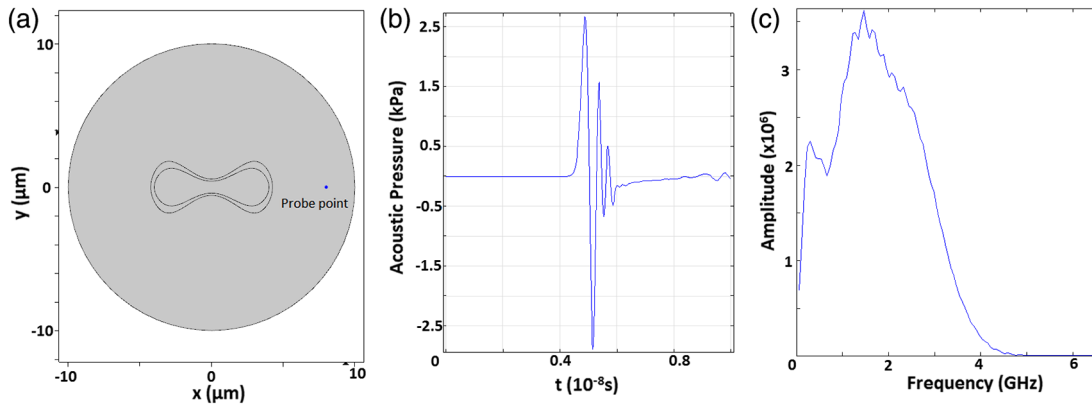


Fig. 7 (a) Location of probe point relative to RBC, (b) PA pressure at probe point versus time, and (c) FFT of the signal showing frequency spectrum of the signal.

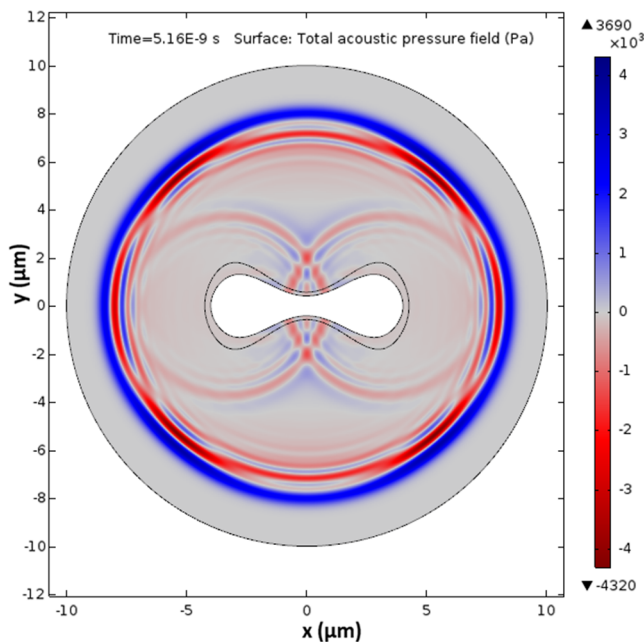


Fig. 8 PA pressure spatial distribution at time of peak amplitude at probe point, RBC shown in white; the remaining area is all modeled as a uniform continuity of water. Units of x and y axes are in μm .

high enough to induce thermal damage in an RBC. This is demonstrated by the fact that a laser focused directly onto the RBC does not display a large temperature change once the heat equation has been solved with FEM.

The PA signal generated by such a pulse was shown to be on the order of kPa, so these simulation results show that the laser should be capable of generating a measurable PA signal while at the same time ensuring that the RBC does not become damaged due to high temperature rises.

These simulations demonstrate the feasibility of an nPAT system to generate PA images of an RBC. Such a system could be used to look into RBCs with high resolution without the need for contrast agents (due to the high absorption coefficient of hemoglobin). We believe that nPAT will be a modality for disease diagnosis and understanding of cell biology at the nanometer-level.

The single-pulse case maximum fluence can be taken to be as high as on the order of 1 kW. In this situation, the ephemeral temperature rise immediately following excitation can be up

to 5 K, but the steady state temperature rise is still quite low. As RBC thermal damage depends greatly on exposure time,³⁰ it is predicted that this should not result in thermal damage to the RBC. However, the instantaneous temperature rise with a MW fluence laser was several hundreds of degrees. Therefore, the maximum fluence for a single pulse should be on the order of 1 kW for the RBC to avoid thermal damage.

The single pulse maximum allowed repetition rate was found to be 100 kHz for a 219-W laser (532 nm and 5-ps pulse duration), with a steady state temperature rise of 3.5 K. In contrast, a femtosecond laser at 830 nm with a repetition rate of 75 MHz was found to induce a temperature rise on the order of 6 K. The absorption of the 532-nm laser is also much larger in hemoglobin, so it could be suggested that the signal generated by each pulse would be of stronger amplitude than in the 830 nm case.

A future direction of this work would be the development of the nPAT system to image RBCs at nanoscale resolutions. Having gained confidence in the thermal safety of the system, we can now proceed to experiment and report on our results after the development of nPAT. nPAT can be employed in the future to image at the nanoscale in 3-D, which has not yet been demonstrated in any ultrasound system. nPAT can be applied to image any cells with appropriate contrast agents (natural or artificial), such as RBCs, cell nuclei, leukemias, anemias, plasmodium infected cells, and more. Currently, we plan to follow up our simulations with experimental results imaging zebrafish RBCs to demonstrate the imaging capabilities of nPAT in biomedical contexts.

Acknowledgments

The authors gratefully acknowledge the Department of Defense Medical Research Programs W81XWH-13-1-0481, the University Strategic Organization (USO) Program at The University of Oklahoma for funding. The authors would like to thank Grace Bouziden and Shanshan Tang for their thorough proofreading.

References

1. R. A. Hoebe et al., "Controlled light-exposure microscopy reduces photobleaching and phototoxicity in fluorescence live-cell imaging," *Nat. Biotechnol.* **25**(2), 249–253 (2007).
2. A. L. Klivanov, "Targeted delivery of gas-filled microspheres, contrast agents for ultrasound imaging," *Adv. Drug Delivery Rev.* **37**(13), 139–157 (1999).

3. T. J. Gould et al., "Nanoscale imaging of molecular positions and anisotropies," *Nat. Methods* **5**(12), 1027–1030 (2008).
4. L. J. Johnston, "Nanoscale imaging of domains in supported lipid membranes," *Langmuir* **23**(11), 5886–5895 (2007).
5. P. Novak et al., "Nanoscale live-cell imaging using hopping probe ion conductance microscopy," *Nat. Methods* **6**(4), 279–281 (2009).
6. H. Shroff et al., "Live-cell photoactivated localization microscopy of nanoscale adhesion dynamics," *Nat. Methods* **5**(5), 417–423 (2008).
7. S. S. Oladipupo et al., "Conditional HIF-1 induction produces multi-stage neovascularization with stage-specific sensitivity to VEGFR inhibitors and myeloid cell independence," *Blood* **117**(15), 4142–4153 (2011).
8. S. Oladipupo et al., "VEGF is essential for hypoxia-inducible factor-mediated neovascularization but dispensable for endothelial sprouting," *Proc. Natl. Acad. Sci. U. S. A.* **108**(32), 13264–13269 (2011).
9. Z. Piao et al., "High speed intravascular photoacoustic imaging with fast optical parametric oscillator laser at 1.7 μm ," *Appl. Phys. Lett.* **107**(8), 083701 (2015).
10. L. Xiang et al., "Noninvasive real time tomographic imaging of epileptic foci and networks," *NeuroImage* **66**, 240–248 (2013).
11. S. Hu et al., "Intravital imaging of amyloid plaques in a transgenic mouse model using optical-resolution photoacoustic microscopy," *Opt. Lett.* **34**(24), 3899–3901 (2009).
12. X. Wang et al., "Noninvasive laser-induced photoacoustic tomography for structural and functional in vivo imaging of the brain," *Nat. Biotechnol.* **21**(7), 803–806 (2003).
13. E. Z. Zhang et al., "Multimodal photoacoustic and optical coherence tomography scanner using an all optical detection scheme for 3D morphological skin imaging," *Biomed. Opt. Express* **2**(8), 2202–2215 (2011).
14. C. P. Favazza et al., "In vivo photoacoustic microscopy of human cutaneous microvasculature and a nevus," *J. Biomed. Opt.* **16**(1), 016015 (2011).
15. S. Hu et al., "Label-free photoacoustic ophthalmic angiography," *Opt. Lett.* **35**(1), 1–3 (2010).
16. S. Jiao et al., "Photoacoustic ophthalmoscopy for in vivo retinal imaging," *Opt. Express* **18**(4), 3967–3972 (2010).
17. L. V. Wang and S. Hu, "Photoacoustic tomography: in vivo imaging from organelles to organs," *Science* **335**(6075), 1458–1462 (2012).
18. S. Danworaphong et al., "Three-dimensional imaging of biological cells with picosecond ultrasonics," *Appl. Phys. Lett.* **106**(16), 163701 (2015).
19. A. G. Doukas, D. J. McAuliffe, and T. J. Flotte, "Biological effects of laser-induced shock waves: structural and functional cell damage in vitro," *Ultrasound Med. Biol.* **19**(2), 137–146 (1993).
20. X. Huang et al., "Determination of the minimum temperature required for selective photothermal destruction of cancer cells with the use of immunotargeted gold nanoparticles," *Photochem. Photobiol.* **82**(2), 412–417 (2006).
21. S. Tang et al., "Transurethral photoacoustic endoscopy for prostate cancer: a simulation study," *IEEE Trans. Med. Imaging* **PP**(99), 1780–1787 (2016).
22. M. Jaunich et al., "Bio-heat transfer analysis during short pulse laser irradiation of tissues," *Int. J. Heat Mass Transfer* **51**(2324), 5511–5521 (2008).
23. H. Park et al., "Characterizations of individual mouse red blood cells parasitized by Babesia microti using 3-D holographic microscopy," *Sci. Rep.* **5**, 10827 (2015).
24. B. T. Cox et al., "Two-dimensional quantitative photoacoustic image reconstruction of absorption distributions in scattering media by use of a simple iterative method," *Appl. Opt.* **45**(8), 1866–1875 (2006).
25. E. Evans and Y.-C. Fung, "Improved measurements of the erythrocyte geometry," *Microvasc. Res.* **4**(4), 335–347 (1972).
26. M. Dao, C. T. Lim, and S. Suresh, "Mechanics of the human red blood cell deformed by optical tweezers," *J. Mech. Phys. Solids* **51**(11–12), 2259–2280 (2003).
27. J. P. Mills et al., "Nonlinear elastic and viscoelastic deformation of the human red blood cell with optical tweezers," *Mech. Chem. Biosyst.* **1**(3), 169–180 (2004).
28. C. Pozrikidis, "Resting shape and spontaneous membrane curvature of red blood cells," *Math. Med. Biol.* **22**(1), 34–52 (2005).
29. C. Y. Chee, H. P. Lee, and C. Lu, "Using 3D fluidstructure interaction model to analyse the biomechanical properties of erythrocyte," *Phys. Lett. A* **372**(9), 1357–1362 (2008).
30. J. Fildes et al., "Effects of short heat exposure on human red and white blood cells," *J. Trauma* **45**(3), 479–484 (1998).
31. F. Fanjul-Vlez et al., "Thermal damage analysis in biological tissues under optical irradiation: application to the skin," *Int. J. Thermophys.* **30**(4), 1423–1437 (2009).
32. C. Zhang et al., "In vivo photoacoustic microscopy with 7.6-m axial resolution using a commercial 125-MHz ultrasonic transducer," *J. Biomed. Opt.* **17**(11), 116016 (2012).
33. A. Danielli et al., "Label-free photoacoustic nanoscopy," *J. Biomed. Opt.* **19**(8), 086006 (2014).
34. D. O. Lapotko and V. P. Zharov, "Spectral evaluation of laser-induced cell damage with photothermal microscopy," *Lasers Surg. Med.* **36**(1), 22–30 (2005).

Pratik Samant is a PhD student at the University of Oklahoma.

Jian Chen is a postdoctoral fellow at the University of Oklahoma.

Liangzhong Xiang is an assistant professor at the University of Oklahoma and the head of TRUE lab.